Ultrasmall Palladium Nanoclusters Encapsulated in Porous Carbon Nanosheets for Oxygen Electroreduction in Alkaline Media

Wei Yan,[a] Zhenghua Tang,*[a, b] Ligui Li,[a] Likai Wang,[a] Hongyu Yang,[a] Qiannan Wang,[a] Wen Wu,[a] and Shaowei Chen*[a, c]

Ultrasmall noble-metal nanoclusters have been gaining extensive attention because of their unique catalytic activity. Herein, we describe a facile in situ method for the preparation of palladium nanoclusters encapsulated in porous carbon nanosheets as effective catalysts for the oxygen reduction reaction (ORR) in alkaline media. Structural characterizations through X-ray diffraction, X-ray photoelectron spectroscopy, and transmission electron microscopy studies indicate that the Pd clusters were well incorporated into porous carbon nanosheets. The composition of the nanocomposites was manipulated by varying the initial loading ratio of Pd to carbon nanosheets (Pd/CNS). Among the series of samples tested, the sample at a Pd/CNS ratio of 1:4 (Pd/CNS-20%) exhibited the best ORR activity with the most positive onset potential and largest diffusion-limited current density, which was even superior to that of commercial Pd black, along with remarkable long-term durability. The findings highlight the unique advantages of employing ultrasmall ligand-free palladium clusters as cost-effective ORR catalysts with high efficiency and remarkable stability.

1. Introduction

Nanoclusters represent an emerging type of functional nanoparticles consisting of tens to a few hundreds of constituent atoms (with a typical dimension less than 2 nm), which possess unique physiochemical properties due to the well-known quantum confinement effects.[1–4] In the past decades, noble metal clusters have been gaining extensive attention, thanks to their versatile applications in sensing and labeling,[5] opto-electronics,[6] and catalysis.[7] For instance, exceptional catalytic performance has been found for ultrasmall gold clusters in a variety of reactions including CO oxidation,[8–9] selective hydrogenation,[10–11] epoxidation[12] as well as oxygen reduction reaction (ORR).[13–15] ORR is a key reaction which largely determines the efficiency of metal-air batteries and fuel cells,

and Pt-based nanomaterials have been recognized as the most effective electrocatalysts for ORR.[16–19] However, the applications are hampered by the limited reserve, high costs and low stability of Pt.[20–21]

To mitigate these issues, significant efforts have been devoted to the development of ORR catalysts based on other metals. Among these, palladium has been widely recognized as a promising candidate, thanks to its satisfactory catalytic performance and relatively low costs.[22–30] For example, Xia and coworkers prepared octahedral and cubic Pd nanocrystals (5-6 nm) and found that the ORR activities of Pd catalysts strongly depended on their shape and surface structures.[31] By fabricating a series of Pd nanoparticles of various sizes, Zhou et al. observed that the most favorable particle size for ORR is 5.0-6.0 nm.[32] Thus far, most prior research has been focused on Pd nanoparticles of relatively large dimensions, and studies of ultrasmall Pd clusters with diameter less than 2 nm have been scarce. Recently, Zhao and coworkers prepared well defined thiolate-capped palladium clusters with the average molecular formula of $Pd_{13-17}(SR)_{18-22}$, and such clusters demonstrated apparent ORR activity and enhanced stability with or without ligand in alkaline solutions.[33]

Nevertheless, when palladium nanoparticles or clusters are employed alone as ORR catalysts, the surface ligands may block part of the active sites and impede the electron-transfer kinetics and mass transport of reaction species.[33] Additionally, palladium clusters are prone to aggregation, dissolution, or decomposition during the electrocatalytic process. Therefore, a number of methods have been adopted to produce highly dispersed Pd metal on substrates or carriers such as metal oxides or carbonaceous materials to enhance the structural integrity of the nanoclusters, and the metal-substrate interactions may also be exploited for manipulating the electro-

[a] W. Yan, Prof. Z. Tang, Prof. L. Li, L. Wang, H. Yang, Q. Wang, W. Wu, Prof. S. Chen
New Energy Research Institute, School of Environment and Energy
South China University of Technology
Guangzhou Higher Education Mega Center
Guangzhou, Guangdong 510006 (P. R. China)
E-mail: zhht@scut.edu.cn
shaowei@ucsc.edu
[b] Prof. Z. Tang
Guangdong Provincial Key Lab of Atmospheric Environment and Pollution Control
Guangdong Provincial Engineering and Technology Research Center for Environmental Risk Prevention and Emergency Disposal
South China University of Technology
Guangzhou Higher Education Mega Center
Guangzhou, Guangdong 510006 (P. R. China)
[c] Prof. S. Chen
Department of Chemistry and Biochemistry, University of California
1156 High Street, Santa Cruz, California 95064 (USA)

catalytic activity. For instance, for graphene quantum dots (GQDs) supported palladium nanoparticles, the GQDs defects have been found to promote charge transfer from the metal particles to GQDs, which weakens the interaction with oxygenated intermediate and leads to enhanced ORR activity.[34–35] In another study,[36] Barman and coworkers prepared nanocomposites based on Pd nanoparticles-embedded porous graphitic carbon nitride which exhibited apparent ORR activity and robust stability. Song *et al.* prepared organic polymer derived microporous carbon supported Pd catalysts for ORR, and examined the impacts of frameworks and hetero-atoms.[37]

Herein, we report an in situ method to the preparation of ultrasmall Pd nanoclusters encapsulated in porous carbon nanosheets. Structural characterizations from XRD, XPS and TEM measurements indicate that the Pd clusters were well incorporated into porous carbon nanosheets. The composition of the nanocomposites was manipulated by varying the initial Pd/CNS loading ratio. Among the series of samples tested, the hybrid with a Pd/CNS ratio of 1:4 (Pd/CNS-20%) exhibited the best activity towards ORR with a most positive onset potential and largest diffusion-limited current density, which was even superior to that of commercial Pd black. Furthermore, Pd/CNS-20% also exhibited better long-term durability than Pd black.

2. Results and Discussion

Porous carbon nanosheets were first fabricated and examined by electron microscopic studies. The typical SEM and TEM images of carbon nanosheets can be found in Figure S1. Figure S2 shows the corresponding nitrogen adsorption/desorption isotherm, and the specific surface area and average pore size of the as-prepared carbon nanosheets were calculated to be 1517.3 m^2g^{-1} and 3.5 ± 0.4 nm, respectively. The Pd/CNS composites were then prepared at varied Pd:CNS feed ratios through an in situ approach, and examined by SEM and TEM measurements. Figure 1 depicts the representative TEM images of the Pd/CNS nanocomposites, where one can see that the nanoclusters were well dispersed without apparent agglomeration. Statistical analysis based on more than 150 individual particles showed that the average diameter was 1.25 ± 0.39 nm for Pd/CNS-10%, 1.31 ± 0.48 nm for Pd/CNS-15%, 1.55 ± 0.55 nm for Pd/CNS-20% and 1.60 ± 0.38 nm for Pd/CNS-25%, all smaller than 2 nm.[38–39] In addition, high-resolution TEM studies (Figure S3) showed well-defined lattice fringes of the Pd nanoclusters where the lattice spacing of 0.22 nm was consistent with the Pd(111) interplanar distance.[37]

Further structural insights were obtained by XRD and XPS measurements. From the XRD patterns in Figure 2, one can see that the carbon nanosheets exhibited two broad peaks at $2\theta = 29.1°$ and 42.5°, which are ascribed to the (002) and (101) crystal planes of hexagonal carbon (JCPDS card# 75-1621), respectively. For the Pd/CNS composites, four additional diffraction peaks can be readily identified at $2\theta = 40.1°$, 47.7°, 68.1°, 82.1° (JCPDS card# 46–1043), due to the Pd(111), (200), (220), (311) diffractions. Notably, the palladium diffraction peaks are markedly broadened, as compared to those of larger
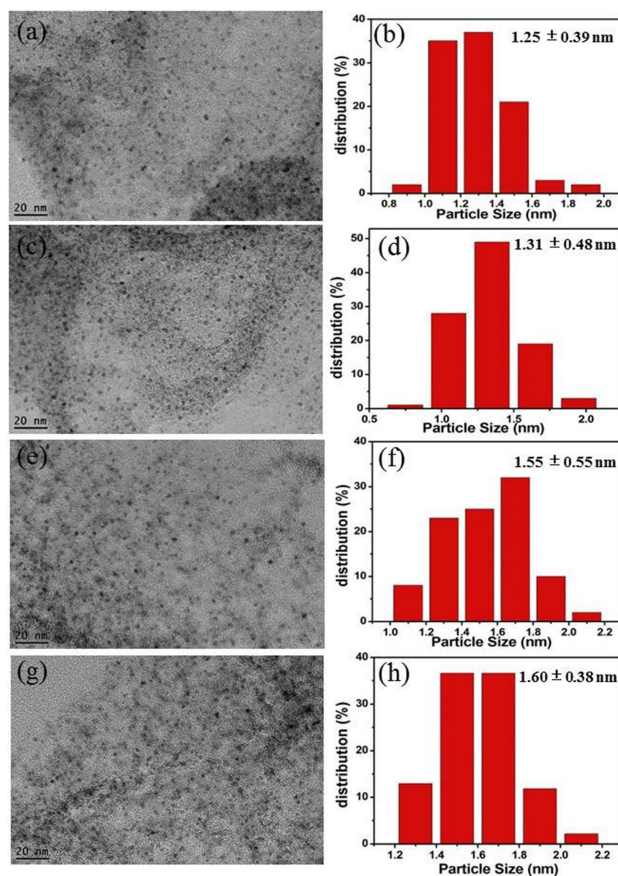

Figure 1. Representative TEM images and corresponding size-distribution histograms of Pd/CNS-10% (a, b), Pd/CNS-15% (c, d), Pd/CNS-20% (e, f), and Pd/CNS-25% (g, h). Scale bars are all 20 nm.
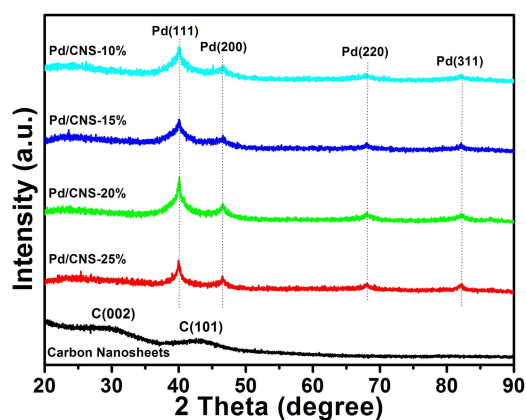

Figure 2. XRD patterns of Pd/CNS-10%, Pd/CNS-15%, Pd/CNS-20%, Pd/CNS-25% and carbon nanosheets.

palladium nanoparticles (5 nm in diameter).[37] These results confirm that the Pd nanoclusters were indeed incorporated and uniformly encapsulated into the carbon nanosheets.

The elemental compositions and valence states were then studied by XPS measurements, Figure S4 depicts the survey spectra of Pd/CNS-10%, Pd/CNS-15%, Pd/CNS-20% and Pd/CNS-25%. In addition to the C 1s (284.8 eV) and O 1s (531.7 eV)

peaks from the carbon nanosheets, signals from Pd 3d can be identified. Based on the integrated peak areas, the mass loading of Pd in the series of nanocomposites was estimated to be 8.98% in Pd/CNS-10%, 12.98% in Pd-CNS-15%, 17.07% in Pd/CNS-20%, and 20.63% in Pd/CNS-25% (Table S1). Figure 3
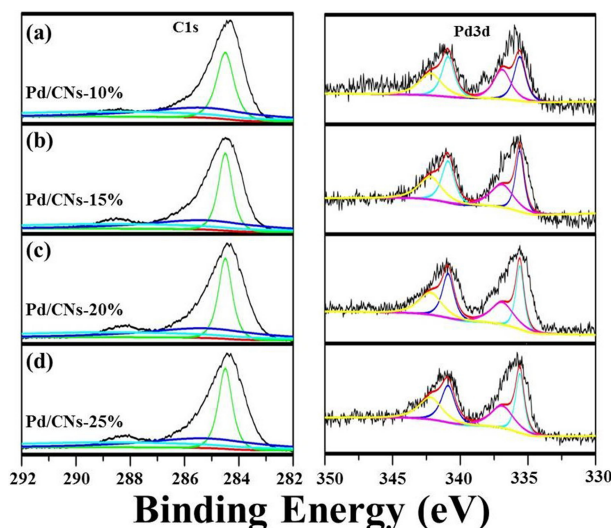

Figure 3. High-resolution XPS spectra of C 1s (left panel) and Pd 3d (right panel) of a) Pd/CNS-10%, b) Pd/CNS-15%, c) Pd/CNS-20%, and d) Pd/CNS-25%.

depicts the high-resolution XPS spectra of the C 1 s and Pd 3d electrons of the series of nanocomposites. In the left panel, deconvolution of the C 1s spectra yields three components, sp^2 carbon (284.5 eV), C in C—O (285.2 eV) and C in C=O/COOH (288.5 eV). In the right panel, the Pd 3d spectra can be deconvoluted into two doublets. The pair at lower energies (335.6 and 340.9 eV) are consistent with those of metallic Pd,[40] whereas those at somewhat higher energies (336.9 and 342.2 eV) could be assigned to Pd(II) species.[35] This suggests the formation of palladium oxide in the samples.[41]

Significantly, the series of Pd/CNS nanocomposites exhibited remarkable electrocatalytic activity toward ORR. The electrochemically active surface area (*ECSA*) of the series of samples were first evaluated (Figure S5)[32] and summarized in Table S2. One can see that with the increase of the initial Pd loading, the *ECSA* increased gradually from Pd/CNS-10% to Pd/CNS-20%, but decreased somewhat with a further increase of the Pd loading in Pd/CNS-25%. For all the samples, the *ECSA* value is more than 150 $m^2 g^{-1}$, much higher than that of Pd black (36.68 $m^2 g^{-1}$); and Pd/CNS-20% displayed the highest *ECSA* value of 186.62 $m^2 g^{-1}$.

Figure 4 shows the RRDE voltammograms of a glassy carbon disk electrode modified with a calculated amount of Pd/CNS-10%, Pd/CNS-15%, Pd/CNS-20%, Pd/CNS-25%, commercial Pd, as well as carbon nanosheets alone in a 0.1 M KOH solution saturated with O_2 at a rotation rate of 1600 rpm. For all the samples, nonzero cathodic currents started to emerge when the electrode potential was swept negatively to $+0.80 \sim +0.90$ V and reached a plateau at potentials more negative
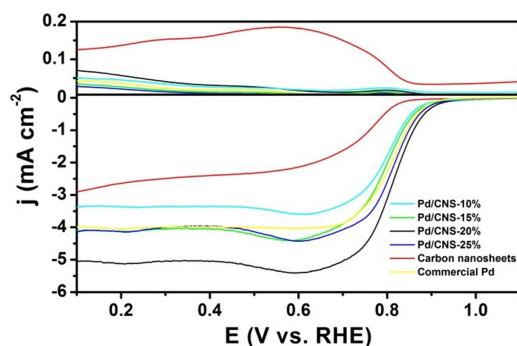

Figure 4. RRDE voltammograms of Pd/CNS-10%, Pd/CNS-15%, Pd/CNS-20%, Pd/CNS-25%, carbon nanosheets and commercial Pd in O_2-saturated 0.1 M KOH at 1600 rpm.

than $+0.6$ V. The onset potential and diffusion-limited current density (at $+0.40$ V and 1600 rpm) can be estimated to be $+0.91$ V and 3.38 $mA\,cm^{-2}$ for Pd/CNS-10%, $+0.92$ V and 4.04 $mA\,cm^{-2}$ for Pd/CNS-15%, $+0.96$ V and 5.03 $mA\,cm^{-2}$ for Pd/CNS-20%, $+0.93$ V and 3.95 $mA\,cm^{-2}$ for Pd/CNS-25% $+0.94$ V and 3.99 $mA\,cm^{-2}$ for commercial Pd, and $+0.85$ V and 2.42 $mA\,cm^{-2}$ for carbon nanosheets. That is, within the present experimental context, the Pd/CNS-20% sample possessed the best ORR activity in the series, which was also attested by cyclic voltammetric (CV) measurements shown in Figure S6.

The ORR activity of the Pd/CNS-20% sample was further examined by CV measurements in both nitrogen- and oxygen-saturated 0.1 M KOH solution at a scan rate of 10 $mV\,s^{-1}$. As shown in Figure 5a, in N_2-saturated 0.1 M KOH solution, only featureless responses were observed in the potential range of -0.05 to $+1.15$ V. However, when the solution was saturated with O_2, a sharp cathodic peak can be readily recognized at $+0.83$ V due to oxygen reduction. The ORR activity of the Pd/CNs-20% sample was then compared with that of commercial Pd black. As shown in Figure 5b, the onset potential of Pd/CNS-20% ($+0.96$ V) was more positive than that of Pd black ($+0.94$ V), along with a greater diffusion-limited current density (at $+0.40$ V and 1600 rpm), 5.03 $mA\,cm^{-2}$ vs 3.99 $mA\,cm^{-2}$.

In the RRDE studies, the number of electron transfer (n) and the yield of H_2O_2 in oxygen reduction process can be calculated by Equations (1) and (2):

$$n = \frac{4I_d}{I_d + I_r/N} \tag{1}$$

$$H_2O_2 = \frac{200I_r/N}{\frac{I_r}{N} + I_d} \tag{2}$$

in which I_d is the disk current, I_r is the ring current, and N is the collection efficiency of RRDE (0.37 in the present study). The calculated n values can be found in Figure 5c, and in the range of 0 to $+0.80$ V, $n = 3.86$–3.98 for Pd/CNS-20%, slightly higher than that of commercial Pd black (3.74–3.97). Meanwhile, the H_2O_2 yield for Pd/CNS-20% was $<10\%$ in the low overpotential range of 0 to $+0.80$ V, close to that of Pd black. Taken together, these results indicate that Pd/CNS-20% stood out as the best
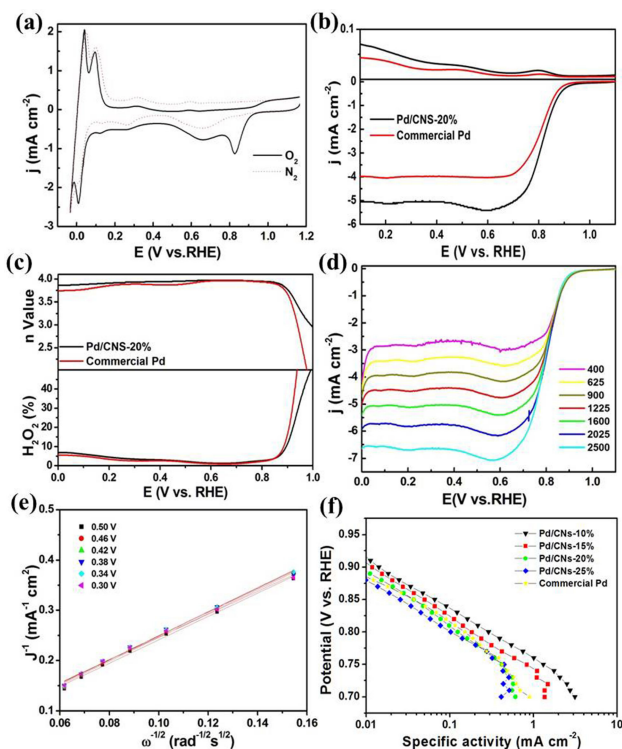
Figure 5. a) Cyclic voltammograms of Pd/CNS-20% in O_2- and N_2-saturated 0.1 M KOH, b) RRDE voltammograms, and c) plots of H_2O_2 yield and number of electron transfer of a glassy carbon electrode modified with Pd/CNs-20% and commercial Pd black catalyst in O_2-saturated 0.1 M KOH solution. Statistic results were based on data of three repeated measurements. d) LSV curves for Pd/CNS-20% at rotation rates of 400 to 2500 rpm. e) Corresponding K–L plots for Pd/CNS-20% at different potentials. f) Corresponding Tafel plots of Pd/CNS-10%, Pd/CNS-15%, Pd/CNS-20%, Pd/CNS-25%, and commercial Pd black. All measurements were conducted with a catalyst loading of 80.8 $\mu g\,cm^{-2}$ in an O_2-saturated 0.1 M KOH aqueous solution at a potential scan rate of 10 $mV\,s^{-1}$.

catalyst among the series toward ORR, and its activity was better than that of commercial Pd black.

The ORR kinetics may be further analyzed by using the Koutecky–Levich (K–L) Equation (3)[42]

$$\frac{1}{i} = \frac{1}{i_k} + \frac{1}{1_d} = \frac{1}{nAFkC_0} + \frac{1}{0.62nFAD_0^{2/3}\omega^{1/2}\nu^{-1/6}C_0} \qquad (3)$$

where i is the measured current, i_K and i_d are the kinetic and diffusion limited current, respectively, ω is the angular velocity of the disk (rad/s), F is the Faraday constant, A is the cross sectional area of the GC electrode (0.2475 cm^2), C_O is the bulk concentration of dissolved O_2 (1.26×10^{-6} mol/cm^3), D_O is the diffusion coefficient of O_2 in 0.1 M KOH (1.93×10^{-5} cm^2/s), v is the kinematic viscosity of the electrolyte solution (0.01 cm^2/s), and k is the electron-transfer rate constant. Figure 5d depicts the RRDE voltammograms of oxygen reduction recorded with the Pd/CNS-20% coated electrode in an O_2-saturated 0.1 M KOH solution at different rotation rates (400 to 2500 rpm). It can be observed that the voltammetric currents increased with the increase of the rotation rate. The corresponding K–L plots are shown in Figure 5e. In the potential range of +0.30 to

+0.50 V, good linearity was observed with a nearly identical slope. Consistent behaviors were observed in the Tafel plots, where the kinetic current density was quantitatively assessed. As shown in Figure 5f, the Tafel slopes were calculated to be 77.02 $mV\,dec^{-1}$ for Pd/CNS-10%, 79.52 $mV\,dec^{-1}$ for Pd/CNS-15%, 78.45 $mV\,dec^{-1}$ for Pd/CNS-20%, 73.53 $mV\,dec^{-1}$ for Pd/CNS-25% and 60.76 $mV\,dec^{-1}$ for commercial Pd black. It is worth noting that all the Tafel slopes are in good agreement with the typical values observed with palladium nanoparticles or nanostructured palladium electrode for ORR.[25,34,43] Furthermore, the close Tafel slopes between the Pd/CNS series and Pd black suggests a similar reaction mechanism for ORR where the first electron reduction of oxygen was likely the rate determining step.[44]

To disclose the cause of the different ORR activity of the series sample, electrochemically active surface area (*ECSA*) measurements were conducted for all the samples. Based on the integrated peak area in Figure S5, the *ECSA* value can be determined by Equation (4):[45]

$$ECSA = \frac{Q_H}{m \times q_H} \qquad (4)$$

Where Q_H is the charge for H_{upd} adsorption, m is the metal loading mass, and q_H is the charge required for monolayer adsorption of hydrogen on a Pd surface (405 $\mu C/cm^2$). Further comparison was made with the specific activity. As shown in Table S2, the specific activity decreased with the increase of the Pd loading in the order of Pd/CNS-20% (115.64 $\mu A\,cm^{-2}$) > Pd black (142.69 $\mu A\,cm^{-2}$) > Pd/CNS-15% (129.08 $\mu A\,cm^{-2}$) > Pd/CNS-25% (119.79 $\mu A\,cm^{-2}$) > Pd/CNS-10% (114.49 $\mu A\,cm^{-2}$). Furthermore, by normalizing the kinetic currents to the corresponding metal mass, the mass activity also varied. All Pd/CNS samples exhibited a mass activity above 170 $A\,g^{-1}$, at least 3 time higher than that of Pd black (52.33 $A\,g^{-1}$), and, again, Pd/CNS-20% exhibited the highest mass activity (286.06 $A\,g^{-1}$).

It is worth mentioning that the ORR activity of the Pd/CNS series is comparable to that observed earlier by Zhao et al. with ultrasmall Pd clusters at 272.4 $A\,g^{-1}$ for ligand-off Pd clusters and 52.9 $A\,g^{-1}$ for ligand-on Pd clusters,[33] but markedly higher than those of Pd nanoparticles of much larger sizes in recent studies in the literature. For example, Huang et al. deposited Pd nanoparticles (average diameter 3 nm) on reduced graphene oxide and the composite exhibited a mass activity of only 88 $A\,g^{-1}$ in 0.1 M KOH.[46] In the study of GQD-supported Pd nanoparticles prepared by Deming *et al.*, the highest mass activity was 20.3 $A\,g^{-1}$.[34] The much lower mass activity is probably due to the much larger Pd nanoparticles (~8 nm).[34]

In the present study, the palladium clusters were synthesized through a direct in situ approach and no ligand was employed. The remarkable activity is probably attributed to the following factors: (a) the ultrasmall Pd clusters possess much higher effective surface area than their larger counterparts;[33] (b) no surface ligand blocking and direct encapsulation in porous carbon nanosheets further enhanced the surface area.

Lastly, the Pd/CNS-20% sample was subjected to long-term durability test in comparison with Pd black. First of all, chronoamperometric measurements were performed at +0.6 V in an O_2-saturated 0.1 M KOH solution. As depicted in Figure 6a,
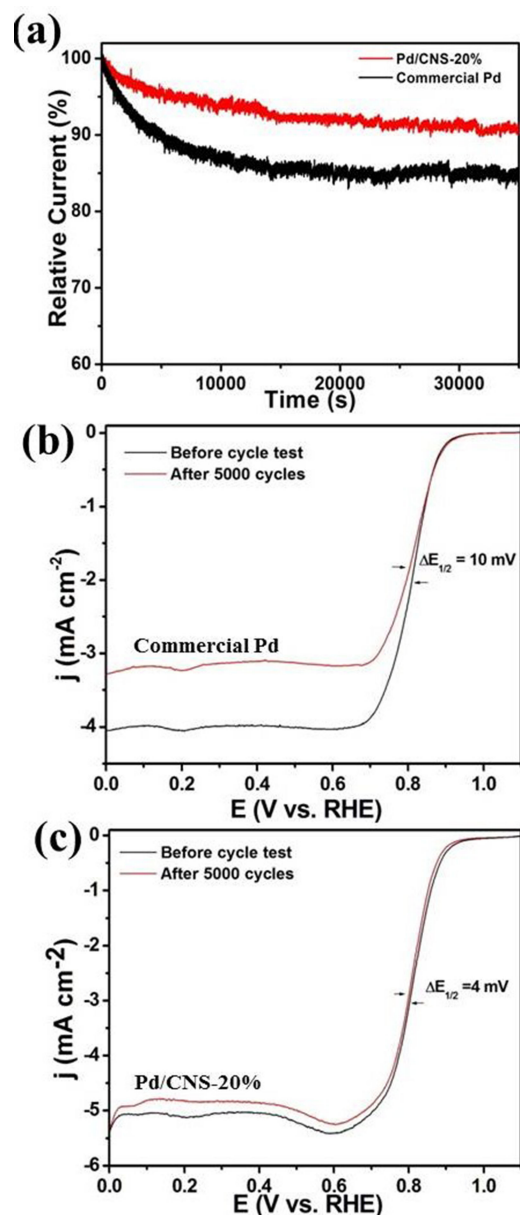

Figure 6. Chronoamperometric responses for ORR at Pd/CNS-20% and commercial Pd black electrodes in an O_2-saturated 0.1 M KOH solution for 35, 000 s (a). The accelerated durability tests (ADTs) of commercial Pd black (b) and Pd/CNS-20% (c) were carried out by before and after 5000 cycles between 0.6 and 1.0 V at a scan rate of 50 mV s^{-1} with a rotation speed of 1600 rpm in an O_2-saturated 0.1 M KOH solution.

the Pd/CNS-20% electrode showed a slow decrease of the current density by about 10% after 35,000 s of continuous operation. However, there was about 16% loss for the commercial Pd black under the same conditions, indicating more robust stability of Pd/CNS-20% for ORR. Secondly, to assess the durability of the catalysts, accelerated durability tests (ADT) were

carried out by cycling the catalyst over the potential range from +0.6 to 1.0 V at 50 mV s^{-1} in an O_2-saturated 0.1 M KOH solution. As shown in Figure 6b, the half-wave potential of commercial Pd black shifted negatively by 10 mV after 5,000 cycles test, while Pd/CNS-20% displayed a much smaller negative shift of only 4 mV (Figure 6c), further attesting the higher durability of Pd/CNS-20% than commercial Pd black. In fact, TEM measurements of the Pd/CN-20% sample after ADT tests (Figure S7) showed that the Pd particles remained well-dispersed and the average diameter (1.70±0.64 nm) was only slightly larger than that before ADT test (Figure 1d). Such remarkable durability may be attributed to the encapsulation of the porous carbon nanosheets that prevented the aggregation of the Pd nanoclusters.[14] Additionally, the porous structure might facilitate the transport of electrolytes as well as reaction intermediates, which was favorable for the reaction kinetics.[47–48]

3. Conclusions

In the present study, a series of Pd/CNS composites were prepared through a facile in situ reduction method and employed as highly efficient catalysts for oxygen electro-reduction. Electrochemical studies showed that Pd/CNS-20% displayed the best activity with the most positive onset potential and largest diffusion-limited current density. The specific activity of Pd/CNS-20% was slightly higher than that of commercial Pd black, while the corresponding mass activity was more than 5 times that of Pd black. Moreover, Pd/CNS-20% demonstrated markedly higher long-term durability than Pd black. The findings highlight the significance of the in situ method as a green and clean technique to achieve atomic economy and for the rational design and preparation of ultrasmall noble metal clusters as cost-effective ORR catalysts with high efficiency and remarkable stability.

Experimental Section

Chemicals

Palladium chloride (PdCl$_2$, 99.9%, Pd > 59.5%, Alfa Aesar), hydrochloric acid (HCl, 36–38%, National Medicines Corporation Ltd. of China), methanol (99.5%, Xinyun Chemical Industry, Tianjin), commercial palladium black (99.99%, Alfa Aesar), zinc nitrate hexahydrate (Zn(NO$_3$)$_2$·6H$_2$O, 99%, Fuchen Reagents, Tianjin), ammonium acetate (NH$_4$OAc, 98%, Fuchen Reagents, Tianjin), cetyltrimethylammonium bromide (CTAB, 99%, Fuchen Reagents, Tianjin), triethylamine (TEA, 99%, Fuchen Reagents, Tianjin) and N, N-dimethylformamide (DMF, 99.5%, Fuchen Reagents, Tianjin) were all used as received without further purification. Water was supplied by a Barnstead nanopure water system (18.3 MΩ·cm).

Preparation of Carbon Nanosheets

Carbon nanosheets were synthesized by following a previously documented protocol.[49–50] Briefly, 60 mmol of $Zn(NO_3)_2 \cdot 6H_2O$ and 20 mmol of terephthalic acid were co-dissolved in 500 mL of DMF in a round bottom flask and stirred at room temperature for 3 h until the solution became colorless. Then the solution was aged at 60 °C for 72 h. After that, 100 mmol of CTAB were added into the solution, and heated at 105 °C for another 90 min under magnetic stirring. Subsequently, 100 mmol of TEA was added quickly and stirred vigorously for 15 min. Precipitates were formed and collected by centrifugation. The precipitates were washed at least three times with copious DMF and chloroform before dried in vacuum at 150 °C for 24 h. The obtained solids were then carbonized under a nitrogen flow at 900 °C for 6 h to produce carbon nanosheets.

In Situ Preparation of Pd Nanoclusters Encapsulated in Porous Carbon Nanosheets (Pd/CNS)

Pd/CNS hybrids were prepared by a modified gas phase reduction method reported in a previous paper.[51] In a typical process, 10 mg of $PdCl_2$ was first dissolved in 20 mL of aqueous HCl (20%) solution at room temperature under vigorous stirring. Then, 24 mg of carbon nanosheets prepared above was added into the above solution under magnetic stirring for 3 h, and subjected to ultrasonic dispersion for 30 min. The solvent was removed from the slurry at 60 °C and dried under vacuum at 60 °C for 12 h. The $PdCl_2$ impregnated carbon nanosheets was heated under an Ar/H_2 (10% H_2) flow at 300 °C for 6 h to reduce Pd(II) to Pd(0) and then cooled down to room temperature under a N_2 flow. The four initial loadings of Pd were used, 10 wt%, 15 wt%, 20 wt% and 25 wt%, and the corresponding final products were denoted as Pd/CNS-10%, Pd/CNS-15%, Pd/CNS-20% and Pd/CNS-25%, respectively.

Characterization and Electrochemical Measurements

The morphology of the samples was examined by a high-resolution transmission electron microscope (JEOL TEM-2010). SEM images were collected with a field-emission scanning electron microscope (FESEM, Merlin). The surface area was determined with a Micromeritics ASAP 2010 instrument with nitrogen adsorption at 77 K using the Barrett–Joyner–Halenda (BET) method. The pore-size distribution was calculated with a DFT method by using the nitrogen adsorption/desorption isotherm and assuming a slit pore model. The surface chemical composition and electronic charge state of the samples were probed by XPS measurements using a VG MultiLab 2000 instrument with a monochromatic Al K_α X-ray source (Thermo VG Scientific). XRD patterns were acquired on a Bruker D8 diffractometer with Cu K_α radiation ($\lambda = 0.1541$ nm).

The electrochemical tests were conducted on a CHI 750E electrochemical workstation (CH Instruments Inc, Shanghai, China) in a 0.1 M KOH aqueous solution at room temperature. A platinum wire electrode was employed as the counter electrode and a Ag/AgCl electrode was used as the reference electrode. The working electrode was a glassy carbon rotating ring-disk electrode (collection efficiency 37%) from Pine Instrument. The working electrode was cleaned with 0.3 μm alumina powder on a polishing mica-cloth (CH instruments Inc) prior to use every time.

Typically, 4 mg of the composite catalysts was first dispersed in 2 mL of anhydrous ethanol, and 20 μL 5 wt% Nafion was added into the mixture and sonicated for about an hour. Then, 10 μL of the mixed solution was dropcast onto the glassy carbon electrode and dried at room temperature. The loading of all catalyst samples on the electrode surface was 80.8 μg cm^{-2}. Cyclic voltammetric (CV) measurements were conducted at a scan rate of 10 mV s^{-1}, and the linear sweep voltammograms (LSV) were collected in an O_2-saturated 0.1 M KOH solution at a scan rate of 10 mV s^{-1} with rotation rates ranging from 400 to 2500 rpm. The current density was calculated based on the geometrical area (0.2475 cm^2) of the working electrode. The electrochemically active surface area (*ECSA*) of the catalysts was measured in a N_2-saturated 0.1 M $HClO_4$ solution at room temperature at a scan rate of 50 mV s^{-1}. Chronoamperometric measurements were conducted in an O_2-saturated 0.1 M KOH solution at +0.5 V for 30,000 s. The accelerated durability test of the catalysts was conducted with the potential cycled in an O_2-saturated 0.1 M KOH solution between +0.6 and +1.0 V at a scan rate of 50 mV s^{-1}. In all tests, the Ag/AgCl reference electrode was calibrated with respect to a reversible hydrogen electrode (RHE). $E_{RHE} = E_{Ag/AgCl} + 0.196\,V + 0.0592\,pH$.

Conflict of Interest

The authors declare no conflict of interest.

[1] R. Jin, C. Zeng, M. Zhou, Y. Chen, *Chem. Rev.* **2016**, *116*, 10346–10413.
[2] S. Wang, H. Yu, M. Zhu, *Sci. China Chem.* **2016**, *59*, 206–208.
[3] R. W. Murray, *Chem. Rev.* **2008**, *108*, 2688–2720.
[4] Y. Lu, W. Chen, *Chem. Soc. Rev.* **2012**, *41*, 3594–3623.
[5] X.-R. Song, N. Goswami, H.-H. Yang, J. Xie, *Analyst* **2016**, *141*, 3126–3140.

[6] O. Varnavski, G. Ramakrishna, J. Kim, D. Lee, T. Goodson, *ACS Nano* **2010**, *4*, 3406–3412.

[7] G. Li, R. Jin, *Acc. Chem. Res.* **2013**, *46*, 1749–1758.

[8] A. A. Herzing, C. J. Kiely, A. F. Carley, P. Landon, G. J. Hutchings, *Science* **2008**, *321*, 1331–1335.

[9] W. Li, Q. Ge, X. Ma, Y. Chen, M. Zhu, H. Xu, R. Jin, *Nanoscale* **2016**, *8*, 2378–2385.

[10] G. Li, C. Zeng, R. Jin, *J. Am. Chem. Soc.* **2014**, *136*, 3673–3679.

[11] Y. Zhu, H. Qian, B. A. Drake, R. Jin, *Angew. Chem., Int. Ed.* **2010**, *49*, 1295–1298.

[12] Y. Liu, H. Tsunoyama, T. Akita, T. Tsukuda, *Chem. Comm.* **2010**, *46*, 550–552.

[13] W. Chen, S. Chen, *Angew. Chem., Int. Ed.* **2009**, *48*, 4386–4389.

[14] Q. Wang, L. Wang, Z. Tang, F. Wang, W. Yan, H. Yang, W. Zhou, L. Li, X. Kang, S. Chen, *Nanoscale* **2016**, *8*, 6629–6635.

[15] L. Wang, Z. Tang, W. Yan, H. Yang, Q. Wang, S. Chen, *ACS Appl. Mater. Interfaces* **2016**, *8*, 20635–20641.

[16] C.-H. Cui, S.-H. Yu, *Acc. Chem. Res.* **2013**, *46*, 1427–1437.

[17] S. Guo, S. Zhang, S. Sun, *Angew. Chem., Int. Ed.* **2013**, *52*, 8526–8544.

[18] X. Huang, Z. Zhao, L. Cao, Y. Chen, E. Zhu, Z. Lin, M. Li, A. Yan, A. Zettl, Y. M. Wang, X. Duan, T. Mueller, Y. Huang, *Science* **2015**, *348*, 1230–1234.

[19] L. Bu, N. Zhang, S. Guo, X. Zhang, J. Li, J. Yao, T. Wu, G. Lu, J.-Y. Ma, D. Su, X. Huang, *Science* **2016**, *354*, 1410–1414.

[20] M. Shao, Q. Chang, J.-P. Dodelet, R. Chenitz, *Chem. Rev.* **2016**, *116*, 3594–3657.

[21] M. Liu, R. Zhang, W. Chen, *Chem. Rev.* **2014**, *114*, 5117–5160.

[22] H. Zhang, M. Jin, Y. Xiong, B. Lim, Y. Xia, *Acc. Chem. Res.* **2013**, *46*, 1783–1794.

[23] A. Chen, C. Ostrom, *Chem. Rev.* **2015**, *115*, 11999–12044.

[24] M. H. Shao, T. Huang, P. Liu, J. Zhang, K. Sasaki, M. B. Vukmirovic, R. R. Adzic, *Langmuir* **2006**, *22*, 10409–10415.

[25] N. Alexeyeva, A. Sarapuu, K. Tammeveski, F. J. Vidal-Iglesias, J. Solla-Gullón, J. M. Feliu, *Electrochim. Acta* **2011**, *56*, 6702–6708.

[26] H. Erikson, A. Sarapuu, N. Alexeyeva, K. Tammeveski, J. Solla-Gullón, J. M. Feliu, *Electrochim. Acta* **2012**, *59*, 329–335.

[27] L. Arroyo-Ramírez, R. Montano-Serrano, T. Luna-Pineda, F. R. Román, R. G. Raptis, C. R. Cabrera, *ACS Appl. Mater. Interfaces* **2013**, *5*, 11603–11612.

[28] H. Erikson, A. Sarapuu, J. Solla-Gullón, K. Tammeveski, *J. Electroanal. Chem.* **2016**, *780*, 327–336.

[29] J. Wu, S. Shan, V. Petkov, B. Prasai, H. Cronk, P. Joseph, J. Luo, C.-J. Zhong, *ACS Catal.* **2015**, *5*, 5317–5327.

[30] J. Wu, S. Shan, J. Luo, P. Joseph, V. Petkov, C.-J. Zhong, *ACS Appl. Mater. Interfaces* **2015**, *7*, 25906–25913.

[31] M. Shao, J. Odell, M. Humbert, T. Yu, Y. Xia, *J. Phys. Chem. C* **2013**, *117*, 4172–4180.

[32] W. Zhou, M. Li, O. L. Ding, S. H. Chan, L. Zhang, Y. Xue, *Int. J. Hydrogen Energy* **2014**, *39*, 6433–6442.

[33] S. Zhao, H. Zhang, S. D. House, R. Jin, J. C. Yang, R. Jin, *ChemElectroChem* **2016**, *3*, 1225–1229.

[34] C. P. Deming, R. Mercado, V. Gadiraju, S. W. Sweeney, M. Khan, S. Chen, *ACS Sustain. Chem. Eng.* **2015**, *3*, 3315–3323.

[35] C. P. Deming, R. Mercado, J. E. Lu, V. Gadiraju, M. Khan, S. Chen, *ACS Sustain. Chem. Eng.* **2016**, *4*, 6580–6589.

[36] T. Bhowmik, M. K. Kundu, S. Barman, *Int. J. Hydrogen Energy* **2016**, *41*, 14768–14777.

[37] K. Song, Z. Zou, D. Wang, B. Tan, J. Wang, J. Chen, T. Li, *J. Phys. Chem. C* **2016**, *120*, 2187–2197.

[38] F. P. Zamborini, S. M. Gross, R. W. Murray, *Langmuir* **2001**, *17*, 481–488.

[39] E. Rangel, E. Sansores, *Int. J. Hydrogen Energy* **2014**, *39*, 6558.

[40] C. D. Wagner, W. M. Riggs, L. E. Davis, J. F. Moudler, G. E. Muilenberg, *Perkin-Elmer Corp.: Edern Prairie* **1979**, *MN*, 1979.

[41] C. P. Deming, A. Zhao, Y. Song, K. Liu, M. M. Khan, V. M. Yates, S. Chen, *ChemElectroChem* **2015**, *2*, 1719–1727.

[42] A. J. Bard, L. R. Faulkner, *2nd Edition* **2001**, *Wiley*, New York.

[43] M. Lüsi, H. Erikson, A. Sarapuu, K. Tammeveski, J. Solla-Gullón, J. M. Feliu, *Electrochem. Commun.* **2016**, *64*, 9–13.

[44] C. Song, J. Zhang, *2008th Edition* **2008**, *Springer*, 89–134.

[45] B. Lim, M. Jiang, P. H. C. Camargo, E. C. Cho, J. Tao, X. Lu, Y. Zhu, Y. Xia, *Science* **2009**, *324*, 1302–1305.

[46] Y.-X. Huang, J.-F. Xie, X. Zhang, L. Xiong, H.-Q. Yu, *ACS Appl. Mater. Interfaces* **2014**, *6*, 15795–15801.

[47] K. Yuan, X. Zhuang, H. Fu, G. Brunklaus, M. Forster, Y. Chen, X. Feng, U. Scherf, *Angew Chem., Int. Ed.* **2016**, *55*, 6858–6863.

[48] W. Niu, L. Li, X. Liu, N. Wang, J. Liu, W. Zhou, Z. Tang, S. Chen, *J. Am. Chem. Soc.* **2015**, *137*, 5555–5562.

[49] M. Ma, D. Zacher, X. Zhang, R. A. Fischer, N. Metzler-Nolte, *Cryst. Growth Des.* **2011**, *11*, 185–189.

[50] T. Yoskamtorn, S. Yamazoe, R. Takahata, J.-i. Nishigaki, A. Thivasasith, J. Limtrakul, T. Tsukuda, *ACS Catal.* **2014**, *4*, 3696–3700.

[51] N. Wang, Q. Sun, R. Bai, X. Li, G. Guo, J. Yu, *J. Am. Chem. Soc.* **2016**, *138*, 7484–7487.